



Strength and fragmentation behaviour of complex-shaped catalyst pellets: A numerical and experimental study

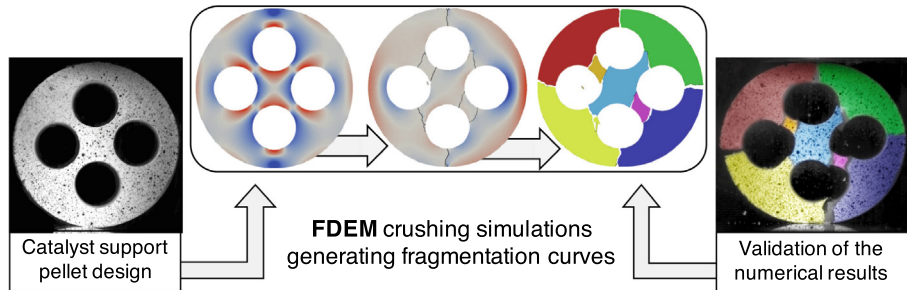
Ado Farsi ^{a,*}, J. Xiang ^a, J.P. Latham ^a, M. Carlsson ^b, E.H. Stitt ^b, M. Marigo ^b

^a Applied Modelling and Computation Group, Department of Earth Science and Engineering, Imperial College London, South Kensington Campus, London SW7 2AZ, United Kingdom
^b Johnson Matthey, P.O. Box 1, Belasis Avenue, Billingham, Cleveland TS23 1LB, United Kingdom

HIGHLIGHTS

- FDEM simulations are verified with disc crushing tests of catalyst support pellets.
- Undetected primary failure in laboratory tests are revealed using FDEM.
- FDEM allows detailed analysis of the fragmentation evolution of pellets.
- Compressive stress concentration in the pellet core generates a greater fraction of fines.
- FDEM reveals pellet shape susceptibility to reactor clogging and pressure drops.

GRAPHICAL ABSTRACT



ARTICLE INFO

Article history:

Received 4 March 2019

Received in revised form 30 October 2019

Accepted 30 November 2019

Available online 6 December 2019

Keywords:

Fracture

Crushing

Simulations

FDEM

Catalyst supports

ABSTRACT

The effects of catalyst support shapes on their final strength and fragmentation behaviour are investigated. Uniaxial compression tests by diametrical loading of solid and four-holed discs with high-speed video recordings are employed to investigate strengths and pellet crushing behaviours. The combined finite-discrete element method (FDEM) is employed to simulate the effects of geometrical features and loading orientation on the pre- and post-failure behaviour of catalysts. A comparison with experimental results is also presented and the remarkable agreement in failure evolution and mode is discussed. A methodology to derive representative fragment size distributions from defined pellet shapes and material properties is introduced, providing a further tool to understand the strength and fragmentation behaviour of catalyst supports. The results suggest that fixed-bed reactors made with solid cylindrical catalysts will be more likely to be affected by pressure drops caused by the choking effect of a significant portion of fines than if it was made with catalyst supports with four holes. Two designs of four-hole catalyst supports sintered with different porosities have also been studied, showing different fragment size distributions and fines production. Characterisation of fines production for different catalyst support designs will improve prediction of reactor clogging and pressure drops.

© 2019 Elsevier Ltd. All rights reserved.

1. Introduction

Particle breakage or structural damage to a pellet, within an accumulation or pack of bodies arises from the complex interaction

between the stress state, environmental conditions, and micromechanical behaviours that are not yet well understood (Tavares, 2007). The degradation and failure of individual elements in a system of bodies is generally the results of different processes. A minor mode of structural damage includes attrition or abrasion, whereby pellets suffer gradual wearing of their surfaces, as a result of stress concentration at certain surface sites, e.g. on the corners,

* Corresponding author.

E-mail address: ado.farsi@imperial.ac.uk (A. Farsi).

edges or protrusions. Only fines are produced in this process, as the parent bodies are left largely intact. A major mode of structural damage called crushing, happens when bodies are subjected to a sufficiently high force and energy for which the material that constitute the bodies fails. In this case, fragments of a significant size compared to the original body are generated, and their size distribution arises from the interaction between the pellet shape, mechanical properties and loading conditions (Unland, 2007). This complex interaction is studied in this work, by means of controlled mechanical tests and numerical simulations.

The catalyst pellets typically employed for fixed-bed reactors in steam reformers contain an active metal component supported on porous materials with a high surface area, e.g. alumina (aluminium oxide, Al_2O_3). To maximise the available surface area and increase heat transfer, these supports can be shaped as cylindrical pellets, balls or more complex configurations. The latest generation of pellets are manufactured by extrusion or pelletisation (i.e. compressing a powder into special holed shaped dies). The sintered pellets are then loaded in bulk with supposed random orientations into 70–130 mm ID alloy tubes of about 14 m length. The catalyst support pellets are packed into tubes through which gases are injected under pressure. In conventional reforming processes, reaction temperatures in the 450–950 °C range are required to drive the endothermic reactions depending on the application (Rostrup-Nielsen and Rostrup-Nielsen, 2002). For this reason the bundles of tubes are suspended in a heated chamber, as shown in Fig. 1, sometimes with some 100–500 tubes per reactor chamber.

Catalyst supports are exposed to various conditions that can compromise their structural integrity. During transport and while introducing catalyst pellets into reactor tubes, they are subjected to dynamic loads, such as vibrations and collisions with neighbouring particles and the container/reactor walls that can chip or break them into pieces. When in service, water might leak into the reactors, permeating the catalysts. Breakage then results from a sudden water expansion and vaporisation out of the pellets pores (Osborne, 2013; Farnell and Carlsson, 2014).

The catalyst support ability of absorbing strains without crushing into small fragments is another key aspect to ensure their performance. For example, during start-up and shutdown cycles, the different thermal expansion properties between the reactor tube and ceramic pellet induces a radial contraction of each section of the catalyst bed. During each cycle, some of the catalyst pellets will rearrange their relative positions to accommodate the reactor contractions. Some pellets will be compressed to failure by the reactor tube and the neighbouring pellets. The size distribution of the frag-

ments produced with this process is related to the catalyst shape and mechanical properties.

The accumulation of these fragments can cause local clogging action and potentially increase pressure drops inside the tubes (Wu et al., 2003): at the same time a local decrease in efficiency of the reaction and an increase of the temperature occurs, damaging the tube. This may affect the reactor to the point that can require replacement of catalyst pellets prematurely. This recurring event has a significant negative impact on plant lifecycle costs (costs for replacements and missing production during the plant downtime). Tubes overheating by just 20 °C can half the tube life, and tube damage and splitting can lead to premature shut down and more frequent, e.g. 3–5 year retubing (costs estimated at \$10–15 M) compared with a more typical 10 year retubing (Stitt et al., 2016). In addition to recognition of the need to minimise local thermal fluctuations, engineers have also turned to steel manufacturers to develop even more highly performing temperature resistant steels (Tancret et al., 2018). A better understanding of fracture propagation in packed structures of ceramic bodies is crucial to the development of new strategies to reduce the accumulation of catalyst fragments and to extend the life-time of reactors, and bring forward further innovations in fixed-bed reactor technology.

Significant recent advancements achieved in the manufacturing technology, including the new opportunities made possible by additive manufacturing (3D printing) allow the production of customised catalyst pellets with complex shapes and architectures. Currently, there are very few methods to assess the strength (Li et al., 2000; Beeckman et al., 2017; David, 2015; Pham et al., 1999) and fragmentation behaviour of complex-shaped catalyst pellets. This work offers some guidance on the design of catalyst supports and pellets in general, introducing a methodology to derive a representative fragment size distribution from defined pellet shape and porosity.

Previous work on comminution of minerals and ores has aimed at modelling fracture and fragmentation of multi-body systems of brittle highly irregular natural shaped particles for the improvement of the design of rock crushers. Discrete element methods (DEM) that handle the interaction between contacts can be adapted to include internal breakage of rigid particles using a range of approximate methods that allow the big ($> 10^6$) particle systems to be modelled for sufficient real time processes of interest. Several DEM breakage models, e.g. the bond breakage models associated with clumped sphere particles (Potyondy and Cundall, 2004) and extended with bounded Timoshenko beams in Brown

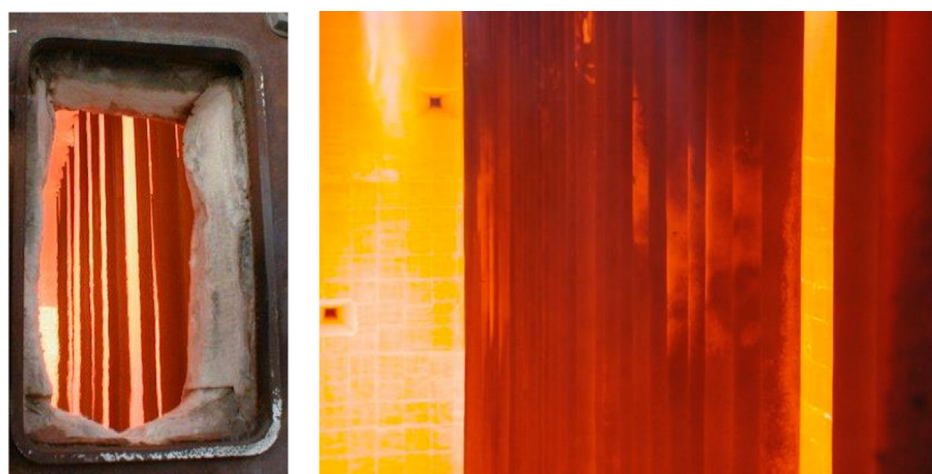


Fig. 1. Reformer with burners and reactor tubes (Stitt et al., 2016).

et al. (2014), the breakage models using polyhedral mesh representations (Kun and Herrmann, 1996), and the parent daughter progeny models (Cleary et al., 2017), have all been proposed and summarised in Jiménez-Herrera et al. (2018). However, for certain applications such as catalyst packs, greater fidelity in the shape and breakage capture is required if void topologies and fragment clogging are to be realistically captured. The ideal approach to model fracture and fragmentation is then a FDEM method, recognising that sufficient computational power will be required to harness these higher fidelity approaches for the target problem. In the first instance, in this paper, the complexity of the multibody behaviour enabled by of FDEM method will not be examined while we focus on modelling the multi-fracturing behaviour for different catalyst shapes and particle structures.

The key features of the two-dimensional combined finite-discrete element FDEM code implemented in Solidity (AMCG, 2018) are the following: (a) compute the contact interaction and motion of bodies, (b) calculate the stresses and deformations and

(c) compute the transition from continua to discontinua when fragmentation occurs. The shape of two-dimensional bodies is discretised through a triangular mesh. Each triangle is both a discrete element (DE) and finite element (FE). When two bodies are in contact, some of the elements of the mesh of the first body overlap some elements of the boundary of the second body, as shown in Fig. 2(a). A contact detection algorithm detects all the couples of DE that are more likely to be in contact, discarding all the couples that are too far to be in contact. This is done to avoid processing the contact interaction of all the possible couple of elements in the system and therefore reducing the run time of the simulation. The contact interaction is implemented through a variational formulation.

This work is organised with the following structure: in Section 2 the confidence in the FDEM capabilities of simulating the failure and fragmentation of porous ceramic pellets is gradually built up with a series of comparisons between experiments and numerical simulations. After a brief overview, Section 2.1 describes the sin-

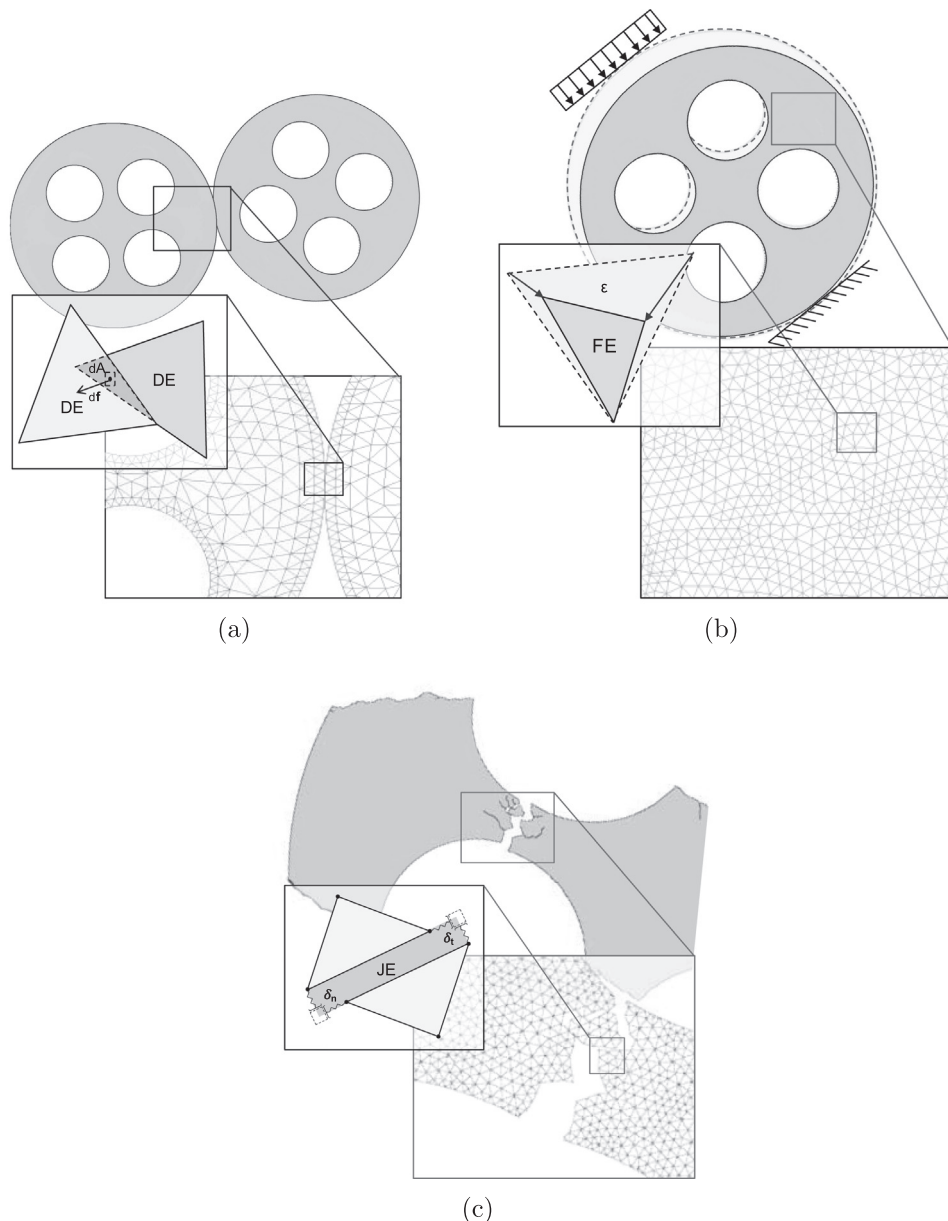


Fig. 2. Scheme of the key features of the Solidity FDEM code: (a) compute the contact interaction and motion of bodies, (b) calculate the stresses and deformations and (c) compute the transition from continua to discontinua when fragmentation occurs.

tering procedure, geometry and bulk density of the tested samples. The mechanical tests performed on the disc-like cylindrical samples with and without holes are introduced in Section 2.2 (Uniaxial compression loading of discs) and Section 2.3 (Nanoindentations). The compression tests are used both to characterise the strength of the two types of ceramic involved in the study (a lower and a higher strength porous ceramic) and set out the tests to be compared with the corresponding numerical simulations. Section 2.4 presents the parameters and boundary conditions employed in the numerical simulations. A comparison between the loads and fragmentation behaviour in the experimental and numerical results is presented and critically discussed in Section 2.5 (Cylindrical pellets) and Section 2.6 (Four-hole pellets). Lastly, in Section 3 the experimental results and numerical simulations on ceramic pellets are used to provide a further tool to understand the strength and fragmentation behaviour of catalyst supports, also introducing a methodology to derive representative fragment size distributions from defined pellet shapes and material properties.

2. Experiments and numerical modelling of catalyst failure

A summary of the mechanical experiments and numerical simulations that have been undertaken for the validation study is shown in Table 1. The variability in the number of tested samples

is due to the limited number of acceptable specimens (i.e. without imperfections) available for this study. The solid cylinder tests together with nano-indentation test are required for characterising the strength and deformability of this ceramic of two different porosities and the parameters needed for the simulations. The four-holed pellet tests were performed to introduce shape and different structural complexity arising from different loading orientations for that shape.

2.1. Sample preparation

Three sets of cylindrical samples with three different geometries were sintered with a reference alpha-alumina powder with an average granulate size in the 170–210 μm range that was compacted at an initial pellet density of 2.25 g/cm³. Two sets consist of cylinders with two different sizes (*Small* and *Big*) and one set consists of cylinders with four holes (*4-hole*). The green pellets are then fired at 1200 °C and 1300 °C to obtain two sets of three group of samples each with different mechanical properties. The average of the diameter of the cylinders (D), diameter of the holes (d), widths (t) and pellet densities of the tested samples are reported in Table 2. Further informations can be found in Farsi et al. (2017).

Table 1
Summary of the experiments and simulations that have been undertaken for the validation study. * Simulation results for the mesh sensitivity have been presented in Farsi et al. (2017). † The four-hole pellets have been tested with nanoindentations.

Set	Size / Orientation	Laboratory experiments	Numerical simulations	
			Nº of tests	Nº of runs
1200 (Low strength)	Big		4	6*
	Small		4	-
1300 (High strength)	Big		6	6*
	Small		5	-
1200 (Low strength)	Weakest orientation (0°)	†	4	1
	Strongest orientation (45°)		4	1
1300 (High strength)	Weakest orientation (0°)	†	3	1
	Strongest orientation (45°)		3	1

Table 2

Average of the measured dimensions and pellet density of the tested specimens.

Set		D [mm]	d [mm]	t [mm]	Pellet density [g/cm ³]
1200	Small	9.59 ± 0.01	-	8.88 ± 0.01	2.21
	Big	18.56 ± 0.01	-	19.16 ± 0.01	2.32
	4-hole	18.39 ± 0.01	5.14 ± 0.01	12.54 ± 0.01	2.31
1300	Small	9.19 ± 0.01	-	8.49 ± 0.01	2.51
	Big	17.69 ± 0.01	-	18.36 ± 0.01	2.69
	4-hole	17.56 ± 0.01	4.88 ± 0.01	12.00 ± 0.01	2.64

2.2. Uniaxial compression loading of discs

Uniaxial compression loading tests were performed on the two sets of discs with and without holes. Prior to testing, one side-face of each specimen had a random speckle pattern applied to the surface. The experiments were recorded with a high-speed video-camera (Vision Research Phantom v12.1 monochrome, maximum capture rate 16,000 frames/s at full-resolution of 1280 by 800 pixels, fitted with a 100 mm macro lens). The optical axis was set normal to the speckled side-face of the specimen. A high-speed video camera was used to capture the post failure behaviour and fragmentation of the samples during the test. The test consists of placing a pellet between two cylindrical plates and diametrically compressing it to failure, i.e. an indirect tensile test known as the Brazilian disc test when applied to solid discs. Since both solid discs and discs with holes are tested in this work, the more generic term ‘uniaxial compression’ is adopted. A monolithic cylindrical plate of aluminium alloy was placed centrally on the stationary base of the test rig (Instron model 5984 electromechanical test frame). An opposing cylindrical loading platen was mounted centrally on the vertically-moving crosshead of the test rig, below the load-cell. During the experiment, the stationary and moving cylindrical plates apply an increasing load to the sample through their flat circular base. The experiments were performed in displacement control, with a crosshead velocity of 10 mm/s. The test rig control software (Instron Bluehill 3) recorded load and displacement during each experiment, at 0.1 s intervals.

The compression on the sample is applied by the two loading plates. These induce on the cylinders without holes a stress field with horizontal tensile stress which, according to a linear elastic

model, has its highest value in the centre of the disc. The tensile strength can be calculated based on the two-dimensional elastic solution for a disc with two concentrated forces applied to its vertical extremes. It is then possible to express the horizontal tensile stress experienced by the specimen in the centre of the disc as a function of the applied load (F) and of the geometry of the sample.

$$f_t = \frac{2F}{\pi D t} \quad (1)$$

Assuming that failure occurs at the point of maximum tensile stress, i.e. at the centre of the disc, the Brazilian test formula (1) gives an estimate of the indirect tensile strength (f_t), where D is the diameter of the disc and t its width (International Society for Rock Mechanics et al., 1978). This relation is only valid for cylinders without holes. With the aim of characterising the tensile strength of the ceramic material comprising the four-hole specimens, cylinders of two different sizes (Small and Big) were tested to take into account the possible variability of the tensile strength of this ceramic material with the different die shapes employed for the green pellet compaction. The mean values and the standard errors of the Brazilian disc test results are shown in Fig. 3(a).

Uniaxial compressive tests were also performed on 6–8 specimens from each of the two sets of four-hole cylinders. When the two hole centres lie directly in line with the loading points, this is the weakest orientation. Considering the angles between the line of the contact points and the symmetry axes of the discs created by the four hole locations, the weakest and the strongest orientations correspond to 0° and 45° respectively. For each set, the four-hole cylinders were tested in both the weakest and the strongest orient-

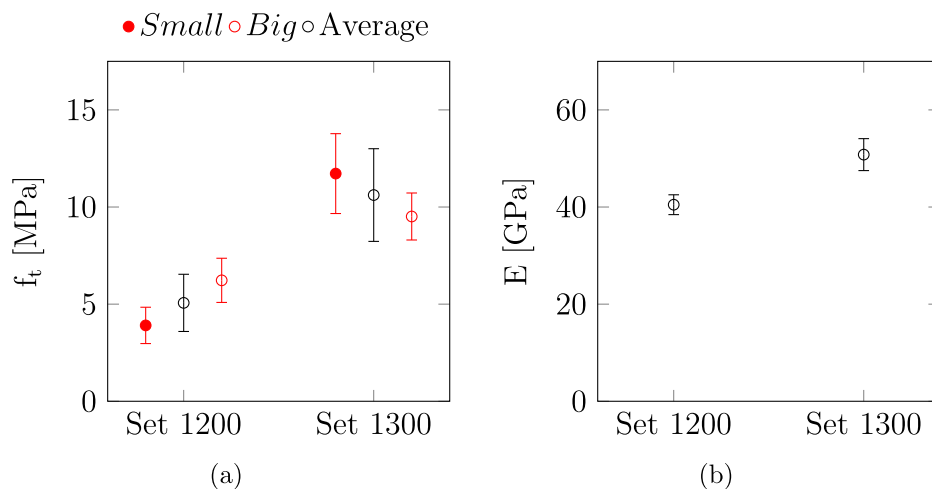


Fig. 3. (a) Indirect tensile strength of the Small (solid red) and Big (void red) cylinders evaluated by Brazilian disc test. Average (black) tensile strength of both Small and Big results calculated for the eight specimens (Set 1200), and eleven specimens (Set 1300). (b) Young's modulus of the four-hole cylinders of the two sets of samples evaluated by nanoindentations. Error bar indicates standard error. (For interpretation of the references to colour in this figure legend, the reader is referred to the web version of this article.)

tation of the holes, as shown in Fig. 4(a) and (b). The mean values and the standard errors of the peak force for each are shown in Fig. 5.

The experimental results can be used to quantify the structurally modified ‘load to failure’, or more simply named ‘equivalent strength’ to highlight the differences in the two loading configurations (weakest and the strongest orientation of the holes), i.e. the maximum value of force that the specimen can support without breaking for a given configuration (orientation) of the load. The results from the other two sets of samples have shown a quite consistent relation between loading orientation, tensile strength and the equivalent strength of the pellets. When normalising the load at failure with the failure load of an equivalent solid cylinder of identical tensile strength and geometry but without holes, all the results converged to a value of about 2% for the weakest orientation (i.e. 1/50 of the cylinder strength without holes) and about 20% (i.e. 1/5) for the strongest orientation. In reconciling the remaining differences between strength reduction due to presence of holes, it is important to point out that the load values at failure have been affected by errors since the video recordings and load cell values were not sufficient to define the exact time and load corresponding to the primary failure of the samples.

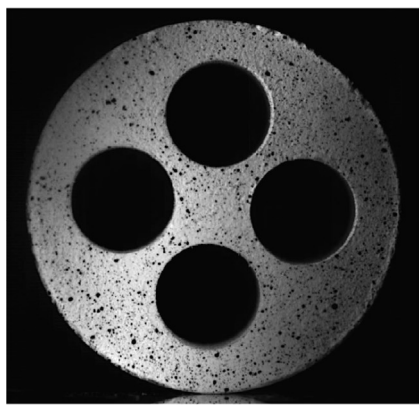
2.3. Nanoindentations

The Young's moduli of the four-hole cylindrical samples were inferred by nanoindentations, with a Nanoindenter XP (MTS

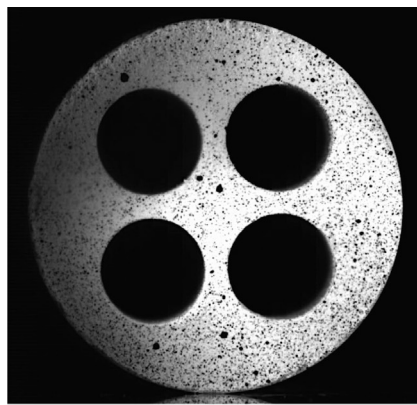
Instruments, UK). The apparatus has maximum load of 400 mN, load noise of < 1 N, μ N, maximum depth of 1,000 nm, and depth noise of < 0.2 nm. A Berkovich diamond indenter with tip radius of < 3 nm has been used to indent the specimen. Each indentation test is performed within 240 s, including a 30 s holding time at the peak load. The testing temperature is maintained within the range 20–22 °C to reduce the thermal drift. For each sample, one hundred indentations have been performed for statistical correction to minimise the experimental error. A correction was performed by excluding the experimental results that were 50% either lower or higher than the average value of the entire distribution (Farsi et al., 2017). The mean values and standard errors of the Young's modulus estimated for each set of specimens are shown in Fig. 3 (b).

2.4. Numerical model

The loading plates and the tested samples have been modelled with 2D FDEM simulations. Both tests and simulations have been performed on discs with and without holes. The two mesh discretisations are shown in Fig. 6(a) and (b) respectively. Note that in anticipation of performing simulations that can capture changes in much shorter than millionths of a second, experiments were also recorded with a high-speed camera to determine the fracture path during crushing. The bottom plate is fixed and the top loading plate is constrained with constant velocity. The velocity of the constraint is set to 0.01 m/s, which is the loading rate that was set in the

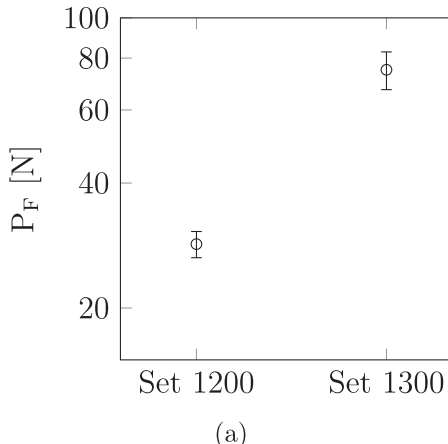


(a)

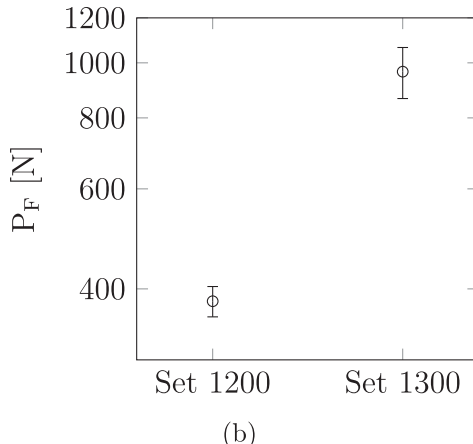


(b)

Fig. 4. Frames from the video recording of the uniaxial compressive tests on four-hole specimens: (a) weakest and (b) strongest loading orientation.



(a)



(b)

Fig. 5. Loads at failure for the uniaxial compressive tests on the four-hole specimens from each set of three specimens: (a) weakest and (b) strongest loading orientation.

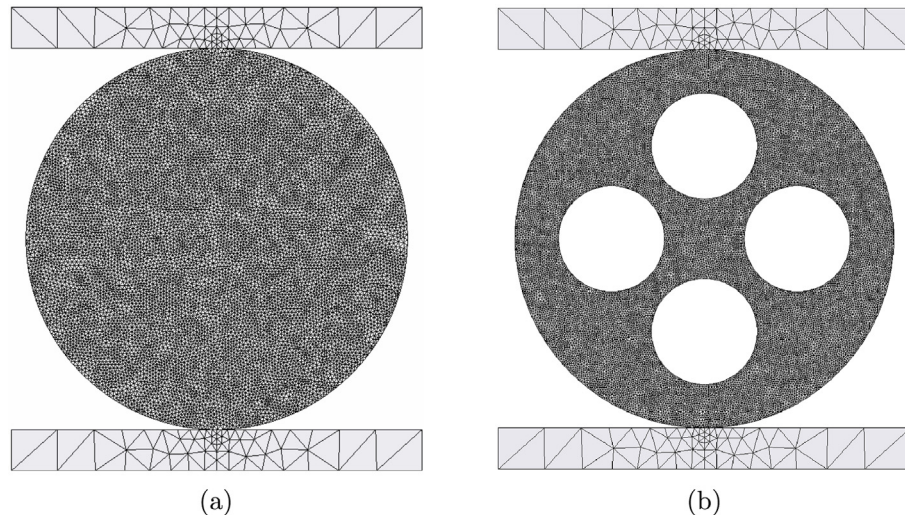


Fig. 6. Simulation of the uniaxial compressive test on a cylinder (a) without and (b) with four holes from Set 1200: triangular mesh discretisation of the specimen and loading plates.

laboratory experiments. To reduce the calculation time, when the simulation starts, the top plate is in contact with the specimen and for this reason an initial velocity equal to the one applied to the experimental constraint is imposed on the simulated loading plates. The specimen is discretised with an unstructured fine mesh to correctly represent both the de-bonding stress during the opening of the crack and the fracture path along the element boundaries. The total number of elements employed in the simulations of discs with and without holes is about 37,000 and 53,000 respectively. The material properties used to describe the loading plates are $E_s=210$ GPa, $\nu_s=0.3$ and $\rho_s=7850$ kg/m³, where E_s is the Young's modulus, ν_s is the Poisson's ratio and ρ_s is the density. The material properties used for the specimens vary depending on the set of the tested sample. The following parameters have been used to simulate the pellets from Set 1200: $E_c=40.5$ GPa, $\nu_c=0.17$, $\rho_c=2310$ kg/m³, $f_t=5.07$ MPa and $G_l=0.20$ J/m². For Set 1300 these were $E_c=57.9$ GPa, $\nu_c=0.17$, $\rho_c=2690$ kg/m³, $f_t=10.62$ MPa and $G_l=0.40$ J/m². Since a value of fracture toughness was not available for the tested samples, the appropriate values for G_l were optimised by trial and error for the large disc for Set 1200 and Set 1300 to ensure the simulation obtained the experimentally observed failure mechanism for the uniaxial compression of a disc. In other words, the optimal value to assign to G_l was selected from the simulation showing a fracture initiating from the centre of the disc and propagating to the two contact points at the top and bottom plates, as shown in Fig. 7. This calibration process set the scene to progress to simulating more complex shaped geometry pellets with the same properties. The same values of energy release rate have been used for the simulations of uniaxial compression of pellets with four holes.

Numerical simulations of the uniaxial compression tests on the disc with four holes have been carried out loading the specimens in different orientations, i.e. with respect to the angles between the line of the contact points and the symmetry axes of the discs created by the four hole locations. Loading orientations at intervals of 5° have been considered between the weakest (0°) and the strongest (45°) orientation configuration of the four-hole disc.

2.5. Cylindrical pellets results

As was pointed out, since a value of fracture toughness was not available for the cylindrical samples, values for G_l were optimised for the two sample sets to obtain the correct theoretical and

observed tensile initiation and failure mechanism for the uniaxial compression of a disc. It is important to point out that the values of G_l deduced in this way as being applicable were lower than the corresponding values obtained in the literature for a similar porous alumina sample. This might be an effect of the procedures that have been employed to sinter the tested samples, as also the tensile strengths and Young's moduli were lower than the corresponding values published in the literature for a similar porous alumina sample. In Fig. 7, a comparison between the numerical simulation and the actual experiment of cylindrical pellet from Set 1200 is presented. Fig. 7(a) shows the horizontal stresses reaching the value of tensile strength (red) in the centre of the disc before failure. After that point, a fracture initiates from the centre and propagates diametrically to the two points of contacts, as shown in Fig. 7(b). While the fracture reaches the two points of contact, also the applied load drastically decreases and the two halves of the disc fragment under the action of the two loading plates as shown in Fig. 7(c). The simulation results can be compared with two frames obtained from the high-speed video recordings of the test of a disc with no holes from Set 1200 shown in Fig. 7(d) and (d). The plate displacement that was measured by the rig during the tests was greatly overestimated, due to the high stiffness of the tested samples, and the consequent self compliance of the test apparatus. Assuming an elastic response of the disc and that the applied load is transmitted by each loading plate on a 200 μm portion of the disc surface ($\alpha \approx 0.6^\circ$), an approximate solution for the relation between the plate displacement and applied load during the test can be defined according to Eq. (2) (Wang et al., 2004).

$$d = -\frac{2P}{\pi Et} \left[(1 - \mu) - \log \left(1 + \frac{4}{\sin^2(\alpha)} \right) \right] \frac{\alpha}{\sin(\alpha)} \quad (2)$$

In Fig. 8 the load-displacement curves calculated in the numerical simulations for Set 1200 and Set 1300 are compared with the corresponding approximated experimental curves. The Young's moduli and poisson's ratios used in Eq. (2) to calculate a good approximation for the corrected force-displacement test results are the same that have been used in the simulations. The two numerical curves match the approximated experimental curves. The simulated force-displacement curve for Set 1300 shows some fluctuations, due to the vibrational modes (mostly rotations) of the specimen during loading. The maximum value for the contact force is slightly higher in the numerical results than in the theoret-

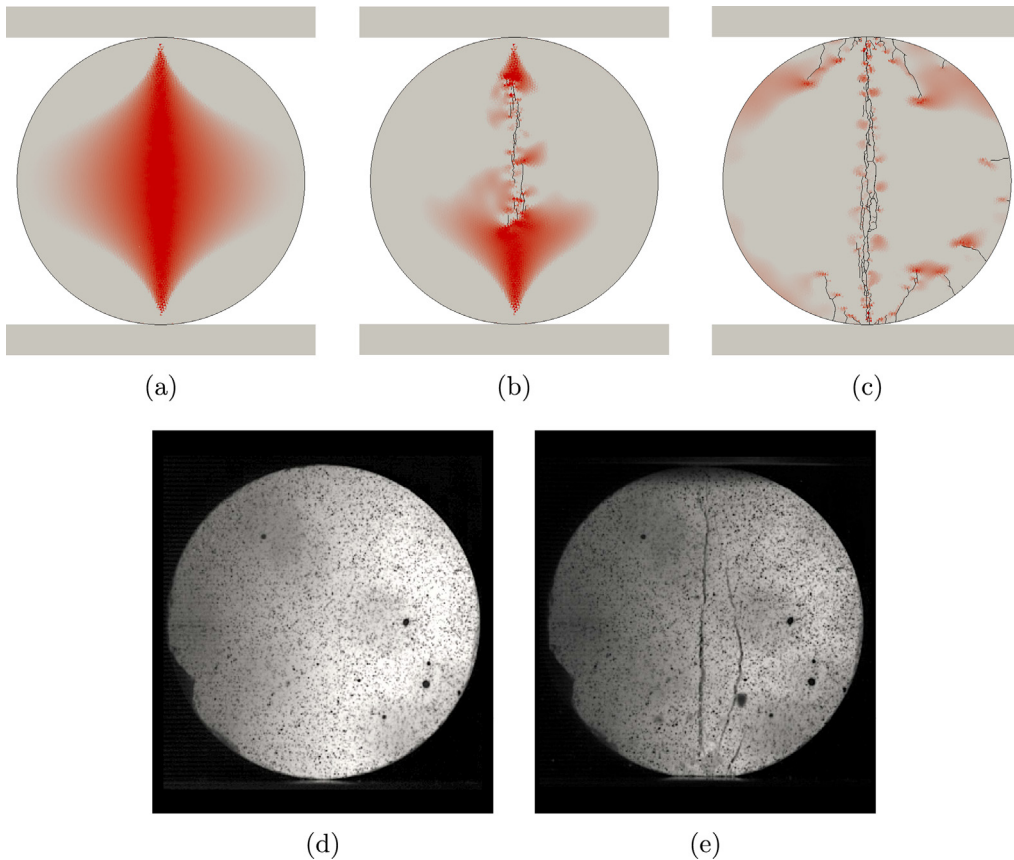


Fig. 7. Simulation of the uniaxial compressive test on a cylinder without holes from Set 1200: (a) Horizontal tensile stress field before failure reaching the value of tensile strength in the centre of the disc. (b) Crack propagating from the centre of the disc to the two sides and (c) splitting of the two sides of the disc after primary failure fragmentation. Two frames from the video recording of the uniaxial compressive test on a cylinder without holes from Set 1200: (d) before and (e) after primary failure.

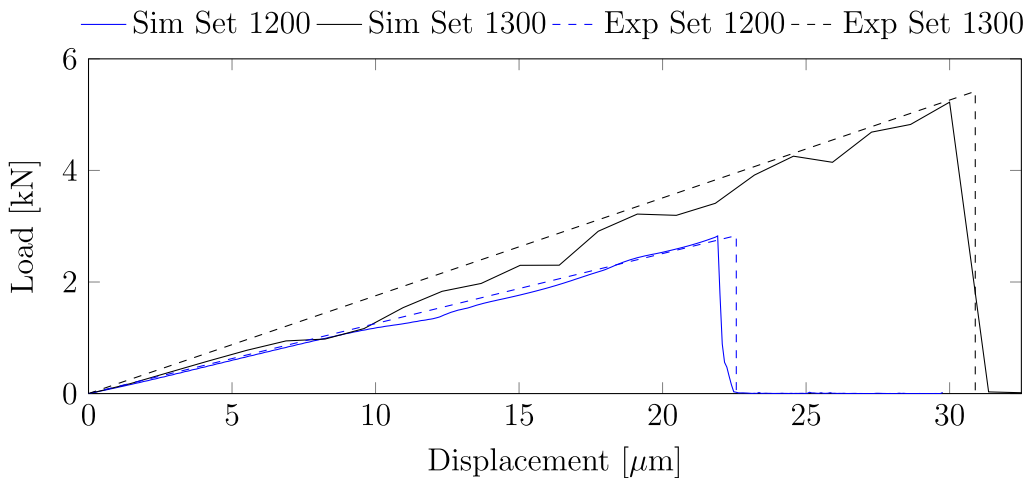


Fig. 8. Force-displacement curve for the uniaxial compressive test on a cylinder without holes from Set 1200 (blue) and Set 1300 (black). Comparison between the numerical results (solid lines) and the theoretical curve given by the experimental results (dashed lines). (For interpretation of the references to colour in this figure legend, the reader is referred to the web version of this article.)

ical prediction obtained from the experimental results. This could be because the mesh elements are not all perfectly aligned across the vertical plane where the stress field develops its maximum tension. A mesh sensitivity analysis has been presented in Farsi et al. (2017), showing that the uniaxial compression results applied to the Brazilian disc example are not particularly sensitive to the mesh size and mesh structure.

2.6. Four-hole pellets results

Due to the limited number of specimens available and the difficulties in keeping pellets held in position with a precise hole symmetry orientation during the tests, catalyst pellets have only been tested in the neighbourhood of the weakest (0°) and strongest (45°) orientations. The experimental results of the uniaxial com-

pressive test on four-hole pellets from Set 1200 in the weakest orientation have been compared with corresponding numerical simulations: Figs. 6(b) and 9(a) respectively, show the triangular mesh discretisation of the specimen and the mean stress field on the four-hole pellet before primary failure. The stress is reaching the value of the tensile strength in various locations around the holes (in red). During the primary fragmentation the propagating fractures splitting the pellet in two halves and fragmenting the core into three chips, as shown in Fig. 9(b). A short time later, initial cracks have propagated from the primary failure, the tensile stress builds up on two opposite holes on the right and left hand side of the pellet, splitting the two halves of the cylinder into smaller fragments. Fig. 9(c) shows the crushed pellet after ultimate failure. Different fragments have been identified with different colours. Fig. 9(d) shows a frame from the video recording of the corresponding actual experiment. The same colour pattern has been applied to help identifying the fragments in the video recording. When the ultimate failure is reached in both the numerical and actual experiment, four bigger fragments on the pellet shell (in red, green, purple and violet) and three smaller in the core (in orange, blue and purple) are formed. The similarity between experimental and numerical results is remarkable, for example in the shape of the central piece broken out when the four holes are all joined by fractures at the end of the simulation as seen in the last frame of the video recordings. Some differences might be caused by the two-dimensional idealisation of the pellet as an homogeneous material. Imperfect contacts between the pellet and the loading plate in the third dimension, small imperfections in the real catalyst and a

slightly tilted initial configuration, have not been captured in the two-dimensional numerical simulation.

As an extension to this validation study, the numerical simulations of the uniaxial compressive test on the four-hole pellets from Set 1200 and Set 1300 have been performed for different hole axes symmetry orientations. Fig. 10(a) and (b) show simulated loading orientations at intervals of 5° between the weakest (0°) and the strongest (45°) orientation configuration of the four-hole pellets. The load-displacement curves for the Set 1200 and Set 1300 are shown in Fig. 10(c) and (e) respectively. For these orientations the primary failure is almost immediately followed by the ultimate failure, as there is no significant increase in the load during crushing after the peak in the load-deflection curves. This means that the fragments resulting from the primary failure are also weak in these loading configurations at the loads they have to sustain immediately post-peak, as shown in the schematic diagram in Fig. 11(a). Fig. 10(d) and (f) show a different behaviour for the 40° and 45° loading orientations, when compared with the orientations between 0° and 35°. As summarised in the schematic diagram in Fig. 11(b), the primary failure happens after the first peak in the load-displacement curve, in the 0–10 μm displacement interval. After that, the fragments resulting from the primary failure are loaded again until they break into smaller fragments. This process can be repeated several times until the ultimate failure is reached, as shown in the post peak behaviour of the load-displacement curves for orientations such as 40° and 45°. Moreover, the load that the fragmented pellets can support after primary failure might increase to two or three times higher than the load that had broken

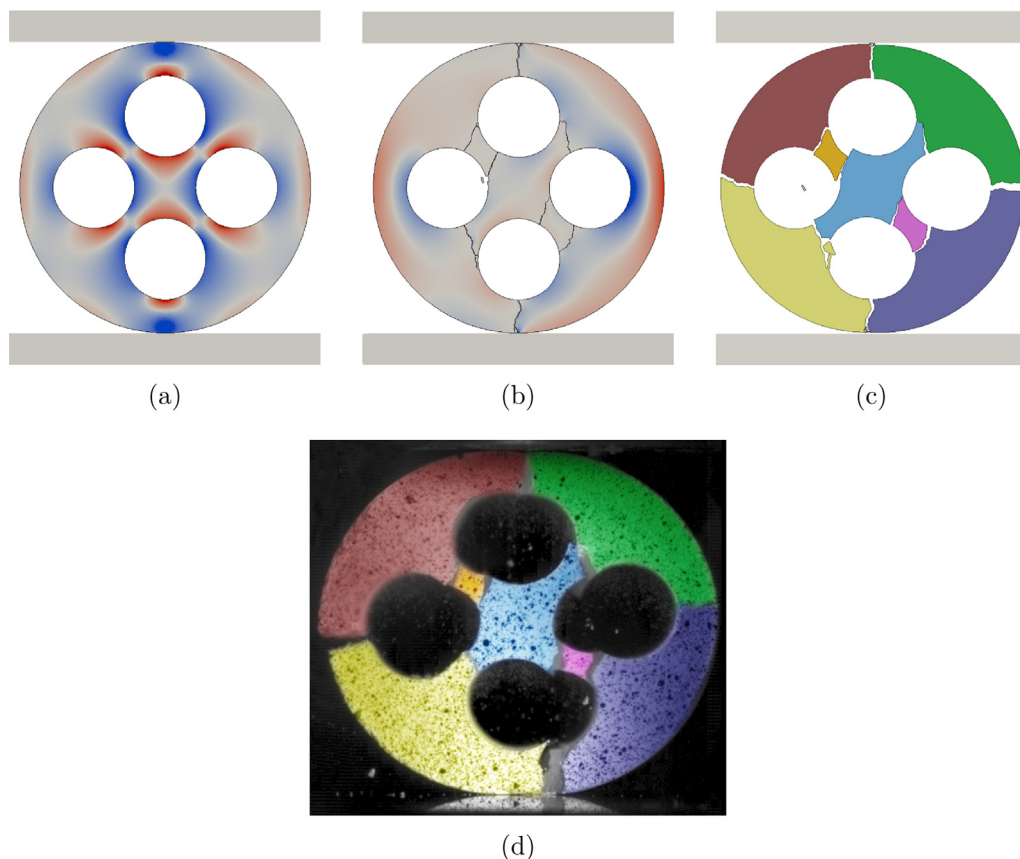


Fig. 9. Simulation of the uniaxial compressive test on a four-hole pellet from Set 1200: (a) Mean stress field on the pellet before primary failure: compressive (blue = -5.07 MPa) and tensile (red = 5.07 MPa) stress. The stress is reaching the value of the tensile strength in various locations around the holes. (b) Mean stress field before the ultimate failure. Initial cracks have already propagated after primary failure and the tensile stress is building up on two opposite holes (right and left hand side) before splitting the two halves of the pellet into smaller fragments. (c) Fragmented pellet after ultimate failure. (d) Frame from the video recording of the uniaxial compressive test on a four-hole pellet from Set 1200 after failure. (For interpretation of the references to colour in this figure legend, the reader is referred to the web version of this article.)

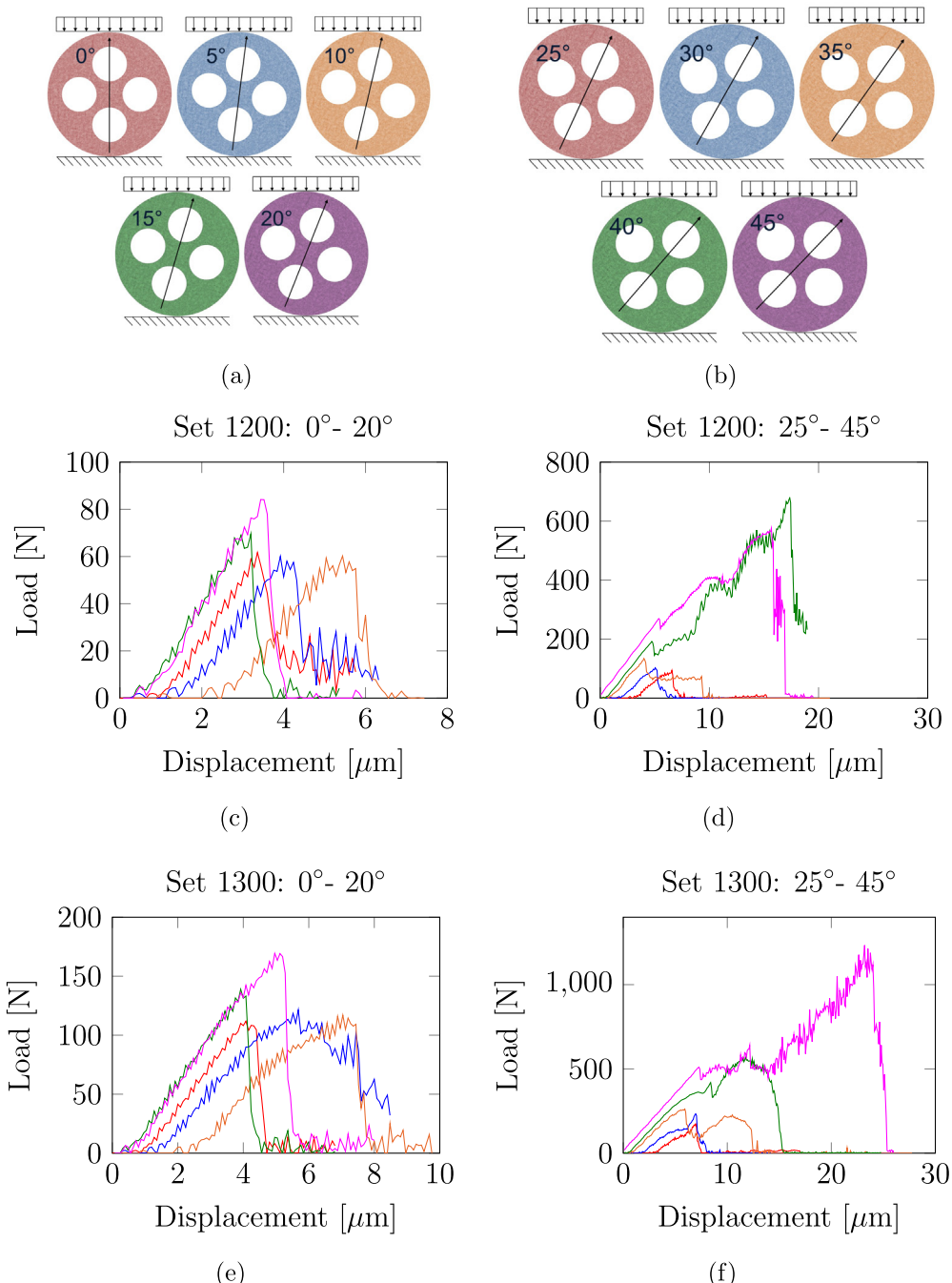


Fig. 10. (a,b) Boundary conditions and load-displacement curves obtained from uniaxial compressive test simulations on the four-hole specimens from (c,d) Set 1200 and (e,f) Set 1300 for orientation angles: (c,e) 0° (red), 5° (blue), 10° (orange), 15° (green), 20° (magenta) and (d,f) 25° (red), 30° (blue), 35° (orange), 40° (green) and 45° (magenta). (For interpretation of the references to colour in this figure legend, the reader is referred to the web version of this article.)

the catalyst in the primary failure. As shown in the schematic diagram in Fig. 11(c), the maximum load supported by the pellets with orientations close to 0° is about one order of magnitude smaller than the ultimate failure load for orientations close to 45°. The differences in the mechanical behaviour that has been illustrated above is due to how different hole orientations induce the maximum principal stress to reach the value of the tensile strength in different directions and locations on the pellet, generating different fracture paths. Moreover, the primary failure load increases from 0° to 45° hole orientation as the direction and location of the induced maximum principal stress diverge from being closer to

the loading plates and perpendicular to the direction of the uniaxial compression. For hole orientations between 0° and 35°, the cracks resulting from the primary failure break the pellet into either two halves, e.g. Fig. 14(a), or three parts, two sides and the core, e.g. Fig. 14(d). When further compressed, the two primary fragments at the sides behave like two arched beams, failing in bending under a relatively low axial load. This process effectively disconnects the pellets from being in contact with the loading plates, reducing the force that is transmitted to the fragments. On the other hand, when the hole orientation is between 35° and 45°, the primary fragments behave like columns that connect the

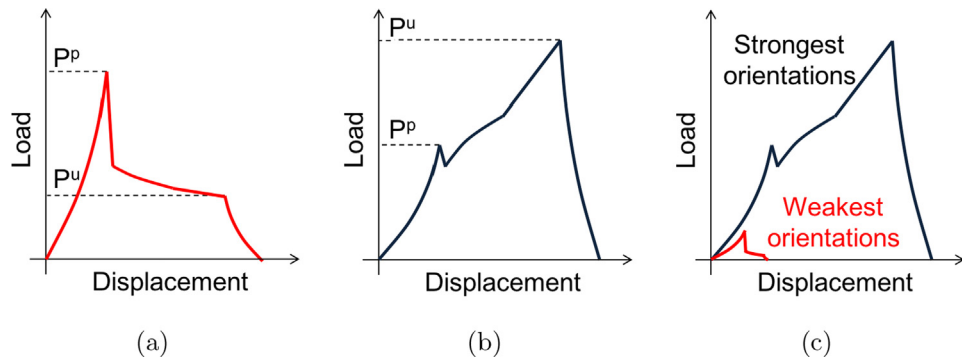


Fig. 11. Schematic diagrams that illustrate the different behaviour of the load-displacement curves for (a) pellets loaded with orientations close to 0° and (b) pellets loaded with orientations close to 45° . (c) Schematic diagram showing that the maximum load supported by the pellets with orientations close to 0° is about one order of magnitude smaller than the ultimate failure load for orientations close to 45° .

two loading plates, allowing the load and the compressive stress to increase to the point of a catastrophic failure that breaks the primary fragments into smaller pieces, e.g. Fig. 14(j).

Fig. 12 shows a comparison between the experimental and numerical load-time curves from the uniaxial compressive test on the four-hole pellets from Set 1200 and Set 1300. The experi-

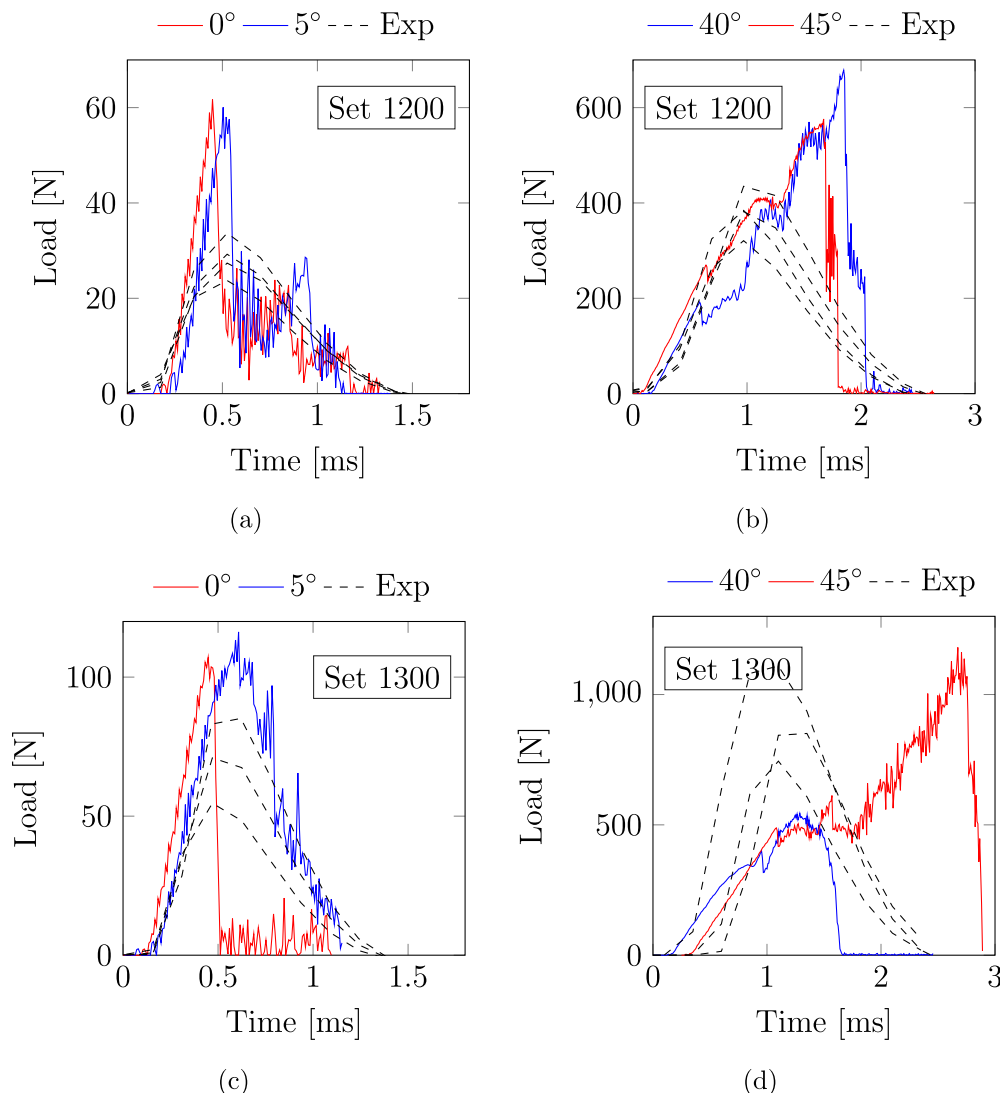


Fig. 12. Comparison of the numerical and experimental compressive test results on the four-hole specimens from Set 1200 (a,b) and Set 1300 (c,d). The experimental results (dashed black) for the (a,c) weakest (0°) and (b,d) strongest (45°) orientations are compared with the numerical compressive test results with orientation angles 0° (red), 5° (blue) and 40° (blue), 45° (red) respectively. (For interpretation of the references to colour in this figure legend, the reader is referred to the web version of this article.)

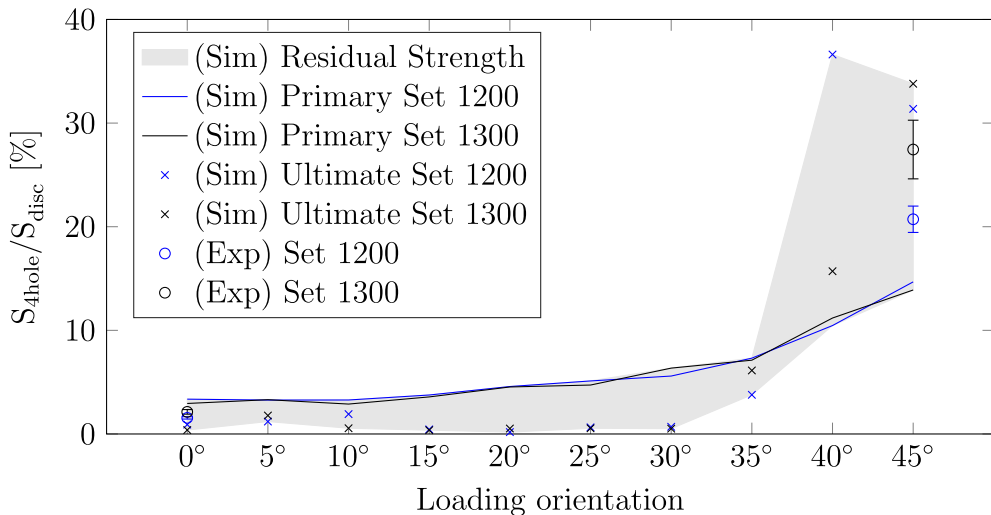


Fig. 13. Relation between the loading orientation and the equivalent strength of four-hole pellets, normalised with respect to the strength of an equivalent cylinder of identical geometry without holes for the two sets of pellets: Set 1200 (blue), Set 1300 (black). Experimental (dots) results for the 0° and 45° loading orientations. Numerical results for the primary failure (continuous lines) and ultimate failure (crosses) for loading orientations between 0° and 45°. The shaded area represents the residual strength after primary failure. The error bars for the experimental data represent the standard error. (For interpretation of the references to colour in this figure legend, the reader is referred to the web version of this article.)

mental results for the pellets in their weakest orientation are compared with the simulated results from loading orientation angles 0° and 5°. This is done to take into account the small rotations of the pellet during the test from their weakest orientation. The numerical results show a higher value of the peak load compared to the experimental peak load for both Set 1200 and Set 1300, as shown in Fig. 12(a) and (c) respectively. This might be due to the lower frequency rate in output from the experimental apparatus or smoothing errors. Moreover, it can be seen that the discrepancy is higher for Set 1200, consisting of weaker pellets, for which failure happens more suddenly. Another important aspect to take into account is the great variability of the experimental results given by the microstructural differences in samples from the same set. Fig. 12(b) and (d) compare the experimental results for the pellets in their strongest orientation with the simulated results from loading orientation angles 40° and 45° for Set 1200 and Set 1300 respectively. Owing to the relatively rapid strain rates in the laboratory, it is suspected that the experimental results are not sensitive enough to resolve the peak corresponding to the pellet's primary failure, showing just a single peak at a higher load, which corresponds to the pellet ultimate failure. This suggests that, if the tests are not designed correctly, a systematic over-estimation of the pellet strength in its strongest orientation would be the result, due to the residual strength of the fragments resulting from primary failure. This aspect is important when uniaxial compression tests are used to evaluate the strength of pellets. Significant fracture propagation as seen in primary failure is revealed through numerical simulations in a manner that cannot normally be revealed through routine tests.

A complex shaped pellet tested in a particular orientation might be met only apparently, as the peak load from the primary failure might be covered by a higher load peak, corresponding to the strength of the fragments and not the actual strength of the pellet.

In Fig. 13 the load at the primary failure calculated in the numerical simulation for the different orientations is compared with the experimental data. The values of load have been normalised with respect to the strength of an equivalent cylinder of identical geometry without holes. This normalisation emphasises the similarity of behaviour plotted here for Set 1200 and Set 1300 in terms of the influence of the hole orientations with respect

to the diametrical loading orientation. The shaded area displays the residual strength after primary failure from the numerical simulations. This residual strength corresponds to the strength of the fragments and not the actual strength of the pellet. While the ultimate failure load for most of the orientations (0°–35°) is lower than the primary failure load, the residual strength of the fragments can be 2–3 times higher for configurations close to the strongest orientation (40° and 45°). The numerical results provide a relation between the loading orientation and the equivalent strength of the four-hole pellets which is consistent between the two sets of samples. As discussed above, the experimental results were only able to capture the ultimate failure load of the pellets. These experimental values are within the range of load of ultimate failure obtained from the numerical simulations and represented in Fig. 13 by the shaded area.

3. Numerical investigation of fragmentation and fines production

An overview of the four-hole pellets fragmentation after primary and ultimate failure by uniaxial compression for different loading orientations is shown in Fig. 14 for Set 1200 and Fig. 15 for Set 1300. The fragments originating from the primary failure have been identified with different colours. The frame to represent the ultimate failure corresponds to a diametral strain $\epsilon_d = 0.17\%$.

The numerical results show that, given the combination of shape and hole symmetry orientation of the catalyst supports in their strongest orientations, a uniaxial compression generates a compressive stress concentration in the pellet core. At ultimate failure, this high compressive stress is released, generating shock waves and crack branching that break the pellet into small fragments and fines. This suggests that catalyst shapes that allow high concentrations of stress, although capable of withstanding higher loads in particular configurations, also tend to break into a larger fractions of fines. The fragmentation behaviour of spherical alumina supports has been investigated in a previous study (Antonyuk et al., 2005). In that study it was also found that, the ultimate failure of spherical catalyst supports generates a large proportion of fine fragments, due to the high compressive stress in the pellet core. In operating conditions like the ones described

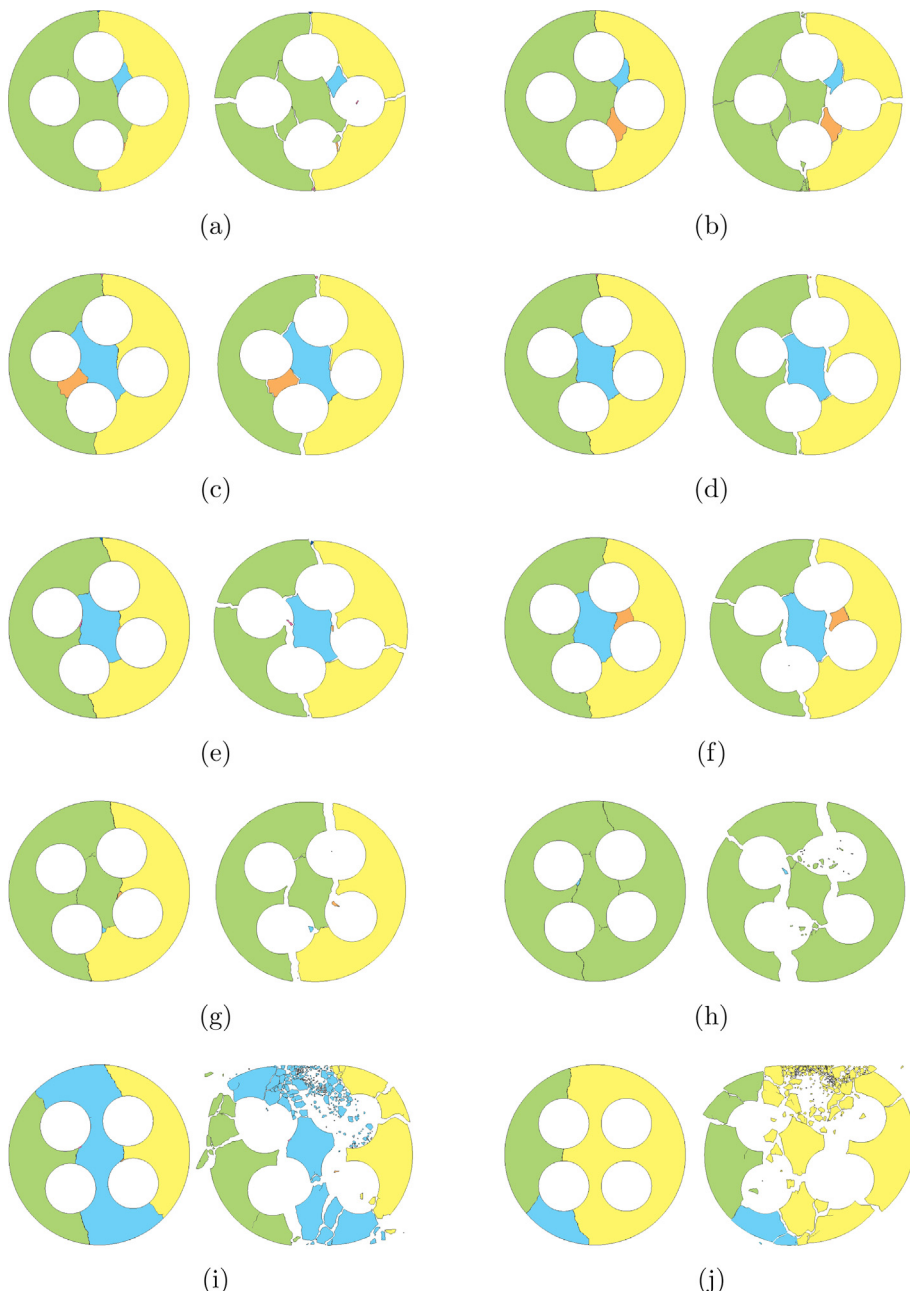


Fig. 14. Comparison of pellet fragmentation after primary and ultimate ($\epsilon_d = 0.17\%$) failure from the uniaxial compressive test simulations on the four-hole specimens from Set 1200 for orientation angles: (a) 0°, (b) 5°, (c) 10°, (d) 15°, (e) 20°, (f) 25°, (g) 30°, (h) 35°, (i) 40° and (j) 45°. Different colours represent fragments after primary failure.

in the Introduction section, the capability of a pellet to withstand a certain load is not relevant given the fact that the external load is simply a function of the final strain applied by a shrinking annulus of the tube walls and the particles' ability to reorientate and slide to less stressed positions in the pack. Improvements in the fragmentation behaviour of catalyst supports can be achieved by avoiding geometrical features that induce stress accumulation, that we have now seen is associated with a larger proportions of fines. This is also confirmed by the experimental results shown in Fig. 16. Pellets loaded in their weakest orientations, with no compressive stress concentration, at ultimate failure produce fewer fine fragments and a few major broken pieces, compared to those loaded in their strongest orientations, which induce compressive stress concentration in the pellet core.

Avoiding the accumulation of fine fragments is crucial for increasing the life-time of the catalyst charge and the reactor steel tubes. This can also help prevent costly operating problems. For this reason the characterisation of the fines produced during crushing of a particular pellet shape and the catalyst support material's strength gives important insights into its performance as a catalyst support. Of course, there are other important aspects that have to be taken into account during the design of a catalyst support other than its fragility due to shape/structure and the ceramic strength itself, such as its surface area, porosity, packing properties, etc. that will all contribute greatly to flow rates pressure drop and reaction efficiency. For instance, a change in the catalyst support shape affects the final fixed bed reactor packing structure, and with a different catalyst porosity (which is related to catalytic activity)

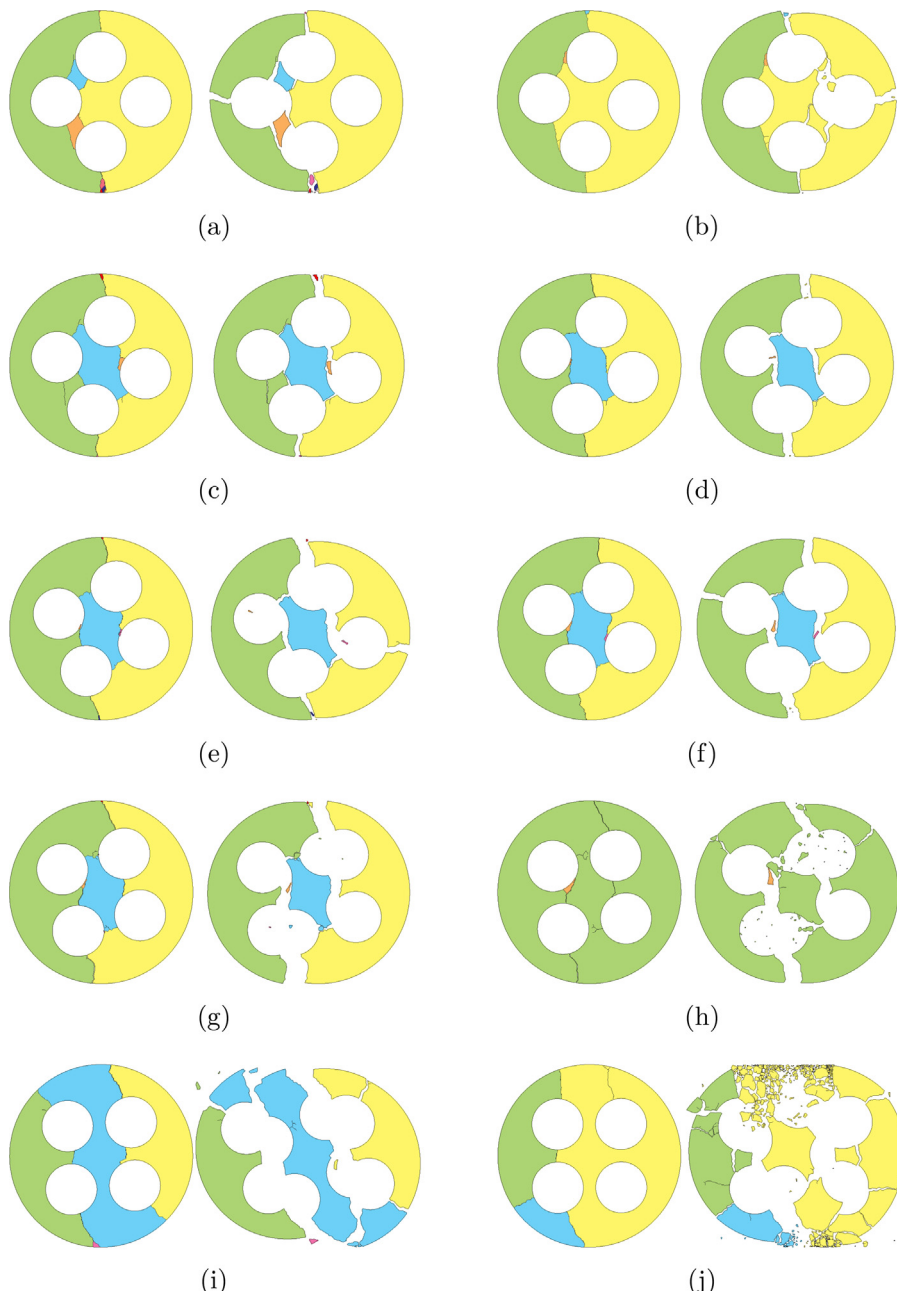


Fig. 15. Comparison of pellet fragmentation after primary and ultimate ($\epsilon_d = 0.17\%$) failure from the uniaxial compressive test simulations on the four-hole specimens from Set 1300 for orientation angles: (a) 0°, (b) 5°, (c) 10°, (d) 15°, (e) 20°, (f) 25°, (g) 30°, (h) 35°, (i) 40° and (j) 45°. Different colours represent fragments after primary failure.

comes a change in strength properties of the ceramic itself. All of this has to be taken into account during design as it may result in poor performances.

Different strategies can be adopted to improve the susceptibility of catalyst supports to the damaging type of fragmentation associated with a large ‘fines production’, such as by a stress-redistribution strategy for shape optimisation. In the event contact forces are sufficient for pellet breakage, the shape would then promote the production of only large broken pieces. This potentially important opportunity requires a little further explanation. To summarise the findings of this research presented above: (a) both quantitative data from numerical simulations and qualitative data from the experiments show that when a pellet is compressed in the

direction of the holes (i.e. 0°, ‘weakest orientation’) a lower fraction of fines is produced. (b) On the contrary, when a pellet is compressed in the direction of the spaces between the holes (i.e. 45°, ‘strongest orientation’) both quantitative data from numerical simulations and qualitative data from the experiments show that a larger fraction of fines is produced. (c) Sets of numerical simulation results of compressions between 0° and 45° show that the transition between the production of a lower fraction of fines and a greater fraction of fines is reached when the combination of the pellet shape and the loading condition generate a high compressive stress concentration in the pellet core. It is in principle perfectly possible to make changes in the design from that of a smooth cylindrical outer contour, i.e. where the contact loads are applied, to one

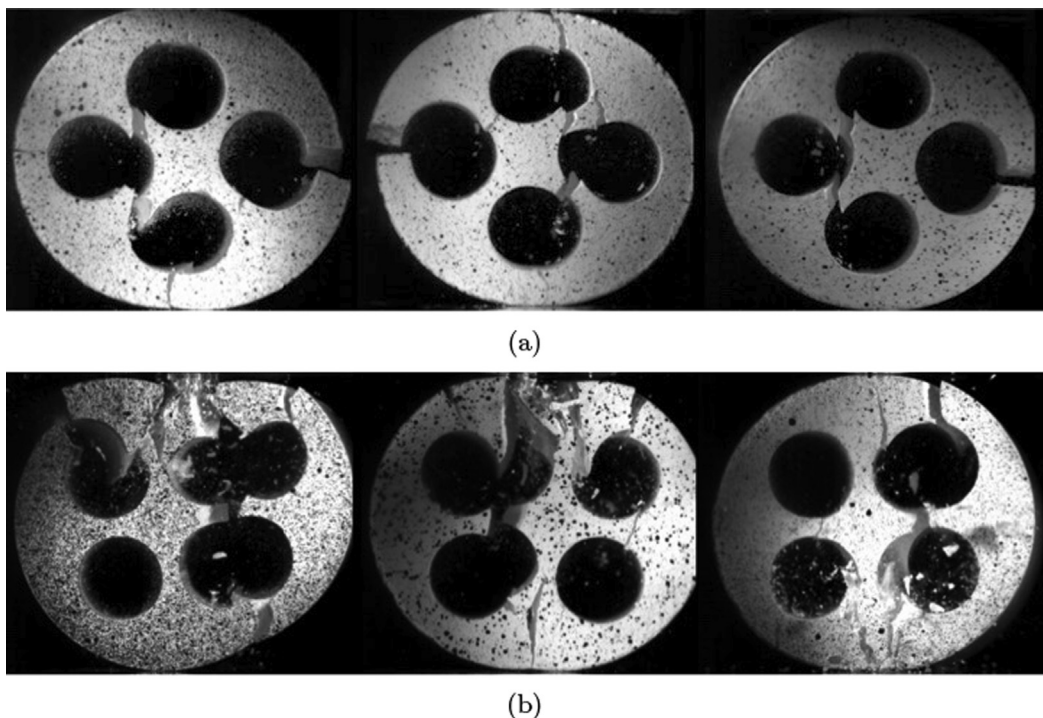


Fig. 16. Frames from the video recordings of the uniaxial compressive tests on six four-hole pellets from Set 1200: (a) three samples loaded in their weakest orientation (0°) and (b) three samples loaded in their strongest orientation (45°).

with an outer contour purposefully designed to redistribute the compressive stress away from the pellet core; for the case in question of a four holed pellet - where load orientations are close to 45° .

Another option is to adjust the sintering process, e.g. by changing the powder size distribution, compaction pressure, firing temperature, etc., to modify the final porosity and strength of the catalyst support, maintaining acceptable levels of catalytic activity. In the present study, the same green pellets have been sintered with two different firing temperatures, producing catalyst supports with different porosities and therefore different mechanical properties. The catalysts from Set 1200 have a higher porosity and weaker mechanical properties than the supports from Set 1300. From a qualitative inspection of the pellet fragmentation it can be noticed that the pellets from Set 1200 are marginally but significantly more fragile (producing more fines) than the pellets from Set 1300. This is particularly noticeable when the pellets are subjected to load orientations close to the strongest hole orientation, i.e. 40° and 45° , in Figs. 14 and 15.

Currently, there are very few methods to compare the strength and fragmentation behaviour of complex-shaped catalyst pellets. For this reason, a methodology for the derivation of representative fragment size distribution curves for the design of catalyst supports from 2D numerical simulations is now introduced for the case of externally cylindrical pellet shapes. To develop the method to compare the fragmentation behaviour of axially symmetric catalyst supports in a reactor tube during thermal contraction, the following observations and simplifying assumptions are made. (i) Pellets with holes tend to be more vulnerable when compressed on a plane normal to their longitudinal axis. For this reason only the loads that are orthogonal to the pellets, axes are considered. (ii) The load transmission between neighbouring pellets is assumed to be higher for two opposite contact points. More complex contact configurations are therefore neglected. (iii) The catalyst pellets in a pack have random orientations and can be compressed by the neighbouring particles and the reactor tube walls with equal likelihood in all orientations. All the possible load-

ing configurations experienced by the pellets in the reactor can therefore be represented by uniaxial compactations between 0° and 45° (for a four-hole pellet). The collection of the fragments produced after primary and ultimate failure for all these simulated compaction orientations are used to define representative fragment size distribution curves for a defined externally cylindrical catalyst support. The area of each fragment obtained from the 2D FDEM simulations is computed and divided by the area of the intact pellet. This allows the calculation of the corresponding normalised mass of the fragments [mass of the fragment/ mass of the intact pellet]. The cumulative size distribution of the fragments produced (i.e. the percentage by total original mass or by total original area in 2D analysis passing a given mass or size of fragment) during crushing simulations are shown in Fig. 17(a) and (b). The plots are compiled using all fragmentation results from the ten representative orientations for the four-hole specimens and the solid cylinders from Set 1200. The two curves are compared in Fig. 17(c) the cumulative distributions after primary and after ultimate failure give the two extreme estimates of the fragment sizes. These extremes may be considered as suitable limits to serve as comparative bounds for consideration of likely fragmentation and fines production during crushing inside a reactor.

Fig. 17(c) shows a comparison of the fragments produced during crushing simulations of ten representative orientations for the four-hole specimens and four realisations of the cylinder without holes from Set 1200. The two catalyst supports show very different fragmentation behaviours. The disk-like cylinder without holes produces a larger fractions of fines both after primary and ultimate failure. A comparison of representative fragment size parameters for the two catalyst shapes is reported in Table 3. In this table, A_{50} is the 50% passing size and A_{10} is the 10% passing size. A_{50} is a typical average area of a fragment whereas A_{10} is the typical area of the finest fraction. For example, if the pellet was originally of area 100 mm^2 , the ultimate typical fragment areas (A_{50}) would be 21.4 mm^2 and 9.5 mm^2 for the four-holed and solid pellets respectively. Similarly, the ultimate typical fines

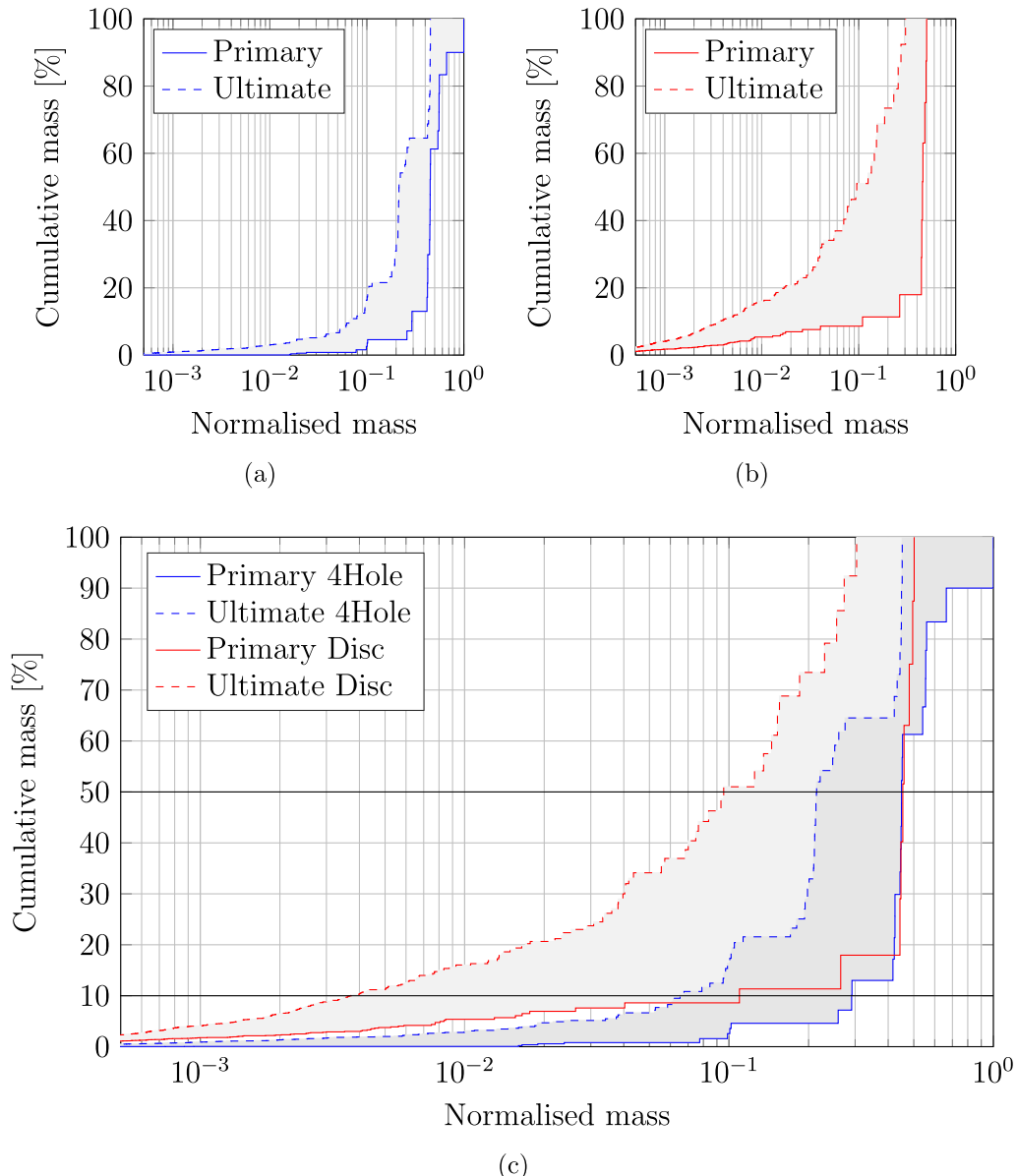


Fig. 17. Cumulative size distribution of the fragments produced during crushing simulations of (a) ten representative orientations for the four-hole specimens (blue) and (b) four realisations of the cylinder without holes (red) from Set 1200. Fragment size distribution after primary (continuous lines) and ultimate (dashed lines) failure. The fragments mass is normalised with the mass of the intact pellet. (c) Comparison between the fragment size distribution curves for the two pellet shapes. The two horizontal black lines highlight the 50% and 10% passing. (For interpretation of the references to colour in this figure legend, the reader is referred to the web version of this article.)

Table 3

Cumulative size distribution of the fragments produced during crushing simulations of ten representative orientations for the four-hole specimens and four realisations of the solid cylinder without holes from Set 1200, see text for further explanation.

Pellet	A_{50}		A_{10}	
	Primary	Ultimate	Primary	Ultimate
Four-hole	0.449	0.214	0.291	0.065
Solid	0.449	0.095	0.109	0.004

fraction areas (A_{10}) would be 6.5 mm^2 and 0.4 mm^2 . In terms of a linear dimension the nominal size of equivalent square fragments, for ultimate failure, would be 4.6 mm and 3.1 mm for the typical average fragment for the four-holed and solid pellets respectively, whereas for the typical fines fraction sizes, the differences are 2.6 mm and 0.6 mm for the four-holed and solid pellets respec-

tively. These fragmentation curves and their derived descriptors of the size distribution strongly suggest that a fixed-bed reactor made with solid cylindrical catalysts will be more likely to be affected by pressure drops caused by the choking effect of a significant portion of fines than if it was made with catalyst supports with four holes. A comparison of the fragmentation behaviour of Set1 and Set2 is also shown in Fig. 18, with yield data plotted in Fig. 3. The two catalyst supports produce a similar fragment size distribution at primary failure, but after ultimate failure, catalyst supports from Set 1200 produce slightly larger fractions of fines, suggesting that they would be more prone to generate pressure drops.

4. Conclusions

The effects of the catalyst support shapes on their final strength and fragmentation behaviour have been investigated. Numerical

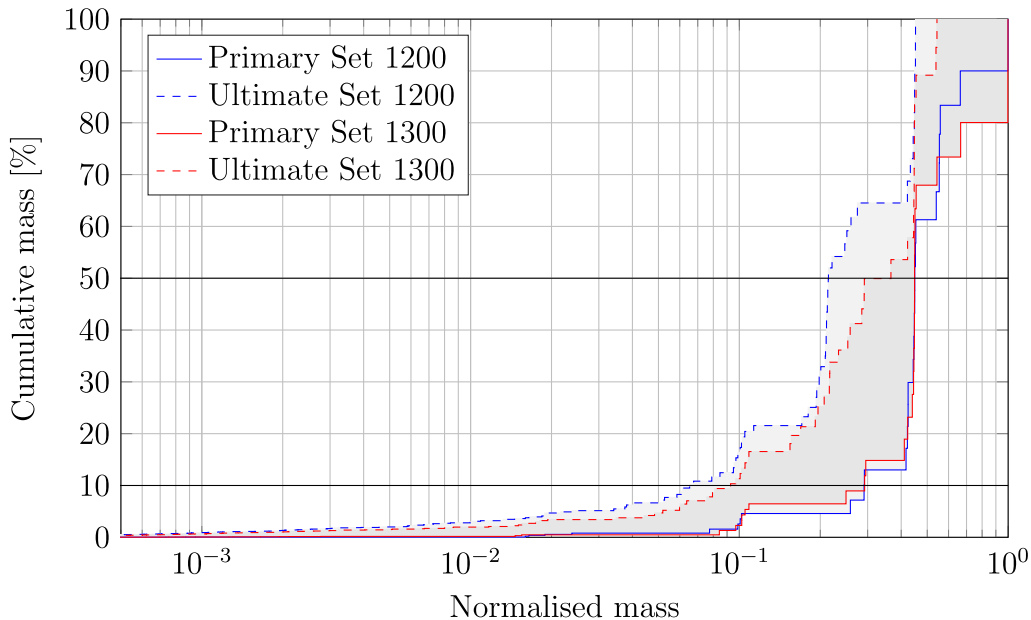


Fig. 18. Cumulative size distribution of the fragments produced during crushing simulations on ten representative orientations for the four-hole specimens from Set 1200 (blue) and Set 1300 (red). Fragment size distribution after primary (continuous lines) and ultimate (dashed lines) failure. The fragments mass is normalised with the mass of the intact pellet. The two horizontal black lines highlight the 50% and 10% passing. (For interpretation of the references to colour in this figure legend, the reader is referred to the web version of this article.)

simulation results of uniaxial compressive tests on disc-like cylinders without holes have been presented. The contact force extrapolated from the numerical simulations has been favourably compared to the corresponding theoretically corrected experimental results. Video recordings from the corresponding experiments provide confirmation of the FDEM code's ability, after calibrating fracture energy release rate for this material, to simulate Mode I fracture as observed in porous ceramic pellet loading tests.

Uniaxial compression laboratory tests on four-hole pellets and high-speed video recordings have been used to estimate pellet strengths and pellet crushing behaviours. Numerical simulations have also been employed to simulate the effects of geometrical features (holes) and loading orientation on the pre- and post-failure behaviour of catalysts. The results have given important indications for the tests that are carried out for assessing the mechanical performance of pellets, showing that depending on how the uniaxial strength test is conducted there is a risk of a systematic overestimation of the pellet strength in its strongest orientation of the holes. This aspect is important when uniaxial compression tests are used to evaluate the strength of pellets. Significant fracture propagation as seen in primary failure is revealed through numerical simulations in a manner that cannot normally be revealed through routine tests.

A comparison with experimental results has been presented and discussed, showing the capability of FDEM numerical simulations to correctly represent the peak loads corresponding to primary and ultimate failure and the fragmentation behaviour of four-hole pellets. A stiffer test apparatus, with higher frequency load transducers and high-speed camera would have to be employed in future studies to improve the quality and the resolution of the experimental data during pellet fragmentation.

A methodology to derive a representative fragment size distribution from defined externally cylindrical pellet shapes and material properties has been proposed, showing the different fragmentation behaviour of the tested catalyst supports.

The presented results strongly suggest that a fixed-bed reactor made with solid cylindrical catalysts will be more likely to be affected by pressure drops caused by the choking effect of a signif-

icant portion of fines than if it was made with catalyst supports with four holes. Moreover, the two four-hole catalyst supports that have been analysed in this work produce similar fragment size distribution curves at primary failure, but after ultimate failure, catalyst supports from Set 1200 produce slightly larger fractions of fines, suggesting that they would be more prone to generate higher pressure drops.

This type of analysis has the potential to promote further innovation in the fixed-bed reactor technology and extend the life-time of the catalyst charge and the reactor by providing important insights for the design of new catalyst pellet shapes and properties. The proposed methodology applied here to axially symmetric pellets, can be extended to any complex-shaped pellet with 3D FDEM simulations since 3D FDEM fracture models have also been developed. This will allow consideration of the range of contact forces active in a real multi-body pack, one not restricted to cylinders and their simplifying assumption that diametral loadings act towards the cylinder's centre.

Experimental data might be employed in future work to further validate the capabilities of the proposed methodology for the generation of fragment size distribution curves from simulation results. For example, digital image correlation methods might be used to separate the fragments and classify them into different categories according to their size ranges. Ideally, attention will be turned to 3D breakage simulations, where size distribution can be compared more easily with experimental results.

Future research will be also undertaken to simulate the whole packed structure of catalysts in fixed-bed reactors, allowing the representation of more realistic pellet loading and tube filling conditions that can help in the study and reduction of damage caused by the crushing behaviour of catalyst supports.

Declaration of Competing Interest

The authors declare that they have no known competing financial interests or personal relationships that could have appeared to influence the work reported in this paper.

Acknowledgement

The authors wish to thank James Bower for the nanoindentation tests and Daniel Curry for his help in sample preparation. This research was supported by the Engineering and Physical Sciences Research Council (EPSRC) with a Case studentship in collaboration with Johnson Matthey and the Impact Acceleration Account grant (Ref: EP/R511547/1).

References

- Applied Modelling and Computation Group (AMCG) at Imperial College London, www.solidityproject.com, 2018.
- Antonyuk, S., Tomas, J., Heinrich, S., Mörl, L., 2005. Breakage behaviour of spherical granulates by compression. *Chem. Eng. Sci.* 60, 4031–4044.
- Beeckman, J.W.L., Cunningham, M., Fassbender, N.A., Datz, T.E., 2017. Length-to-diameter ratio of extrudates in catalyst technology: III. Catalyst breakage in a fixed bed. *Chem. Eng. Technol.* 40, 1844–1851.
- Brown, N.J., Chen, J.F., Ooi, J.Y., 2014. A bond model for DEM simulation of cementitious materials and deformable structures. *Granular Matter* 16, 299–311.
- Cleary, P.W., Sinnott, M.D., Morrison, R.D., Cummins, S., Delaney, G.W., 2017. Analysis of cone crusher performance with changes in material properties and operating conditions using DEM. *Miner. Eng.* 100, 49–70.
- David, E., 2015. Mechanical strength and reliability of the porous materials used as adsorbents/ catalysts and the new development trends. *Arch. Mater. Sci. Eng.* 73, 5–17.
- Farnell, P., Carlsson, M., 2014. The importance of catalyst design in managing the impact of transient operating conditions in ammonia plants. In: AIChE Safety Symposium, pp. 71–82.
- Farsi, A., Xiang, J., Latham, J., Carlsson, M., Stitt, E., Marigo, M., 2017. Does shape matter? FEMDEM estimations of strength and post failure behaviour of catalyst supports. In: 5th International Conference on Particle-Based Methods – Fundamentals and Applications, PARTICLES.
- Farsi, A., Pullen, A.D., Latham, J.P., Bowen, J., Carlsson, M., Stitt, E.H., Marigo, M., 2017. Full deflection profile calculation and Young's modulus optimisation for engineered high performance materials 7, 46190.
- International Society for Rock Mechanics, 1978. Suggested Methods For Determining Tensile Strength of Rock Materials. In: International Society for Rock Mechanics Commission on Standardization of Laboratory and Field Tests, vol. 15, pp. 99–103.
- Jiménez-Herrera, N., Barrios, G.K., Tavares, L.M., 2018. Comparison of breakage models in DEM in simulating impact on particle beds. *Adv. Powder Technol.* 29, 692–706.
- Kun, F., Herrmann, H.J., 1996. A study of fragmentation processes using a discrete element method. *Comput. Methods Appl. Mech. Eng.* 138, 3–18.
- Li, Y., Wu, D., Zhang, J., Chang, L., Wu, D., Fang, Z., Shi, Y., 2000. Extension of a model for bulk crushing strength of spheres to solid catalysts of different shapes. *Ind. Eng. Chem. Res.* 39, 838–842.
- Osborne, S., 2013. Key lessons to optimise ammonia plant performance. *Nitrogen +Syngas* 321, 1–6.
- Pham, H.N., Reardon, J., Datye, A.K., 1999. Measuring the strength of slurry phase heterogeneous catalysts. *Powder Technol.* 103, 95–102.
- Potyondy, D., Cundall, P., 2004. A bonded-particle model for rock. *Int. J. Rock Mech. Min. Sci.* 41, 1329–1364.
- Rostrup-Nielsen, J.R., Rostrup-Nielsen, T., 2002. Large-scale hydrogen production. *CATTECH* 6, 150–159.
- Stitt, H., Liu, L., Wilkinson, S., Dixon, T., Marigo, M., 2016. Application of CFD with DEM to Transport and Reaction Modelling in Catalytic Reactors. In: 1st CFDEM project user meeting.
- Tancret, F., Laigo, J., Christien, F., Le Gall, R., Furtado, J., 2018. Phase transformations in Fe–Ni–Cr heat-resistant alloys for reformer tube applications. *Mater. Sci. Technol. (United Kingdom)* 34, 1333–1343.
- Tavares, L.M., 2007. Chapter 1 breakage of single particles: quasi-static. *Handbook Powder Technol.* 12, 3–68.
- Unland, G., 2007. Chapter 4 the principles of single-particle crushing. *Handbook Powder Technol.* 12, 117–225.
- Wang, Q.Z., Jia, X.M., Kou, S.Q., Zhang, Z.X., Lindqvist, P.A., 2004. The flattened Brazilian disc specimen used for testing elastic modulus, tensile strength and fracture toughness of brittle rocks: analytical and numerical results. *Int. J. Rock Mech. Min. Sci.* 41, 245–253.
- Wu, D., Song, L., Zhang, B., Li, Y., 2003. Effect of the mechanical failure of catalyst pellets on the pressure drop of a reactor. *Chem. Eng. Sci.* 58, 3995–4004.